Supporting Information

Dual passivation strategy based on F/N co-doped coal-based graphene quantum dots for high-efficiency carbon-based perovskite solar cells

Qixu Hu[1,2], Ke Zhao[1], Min Liu[1], Salman Riaz[1],Ying Qi, Peng Wei[1], Jian Cheng[3],Yahong Xie*[,1]

[1] Key Laboratory of Oil & Gas Fine Chemicals, Ministry of Education and Xinjiang Uyghur Autonomous Region, State Key Laboratory of Chemistry and Utilization of Carbon Based Energy Resources, College of Chemical Engineering, Xinjiang University, Urumqi 830017, P. R. China

[2] Zhejiang University-Hangzhou Global Scientific and Technological Innovation Center, Hangzhou 310014, P. R. China

[3] Department of Materials & Chemical Engineering, Hanyang University, Seoul 04763, South Korea

*Corresponding author: Yahong Xie, E-mail: xyh0707@xju.edu.cn

Table of Contents

1、Experimental Section

1.1 Materials

Lead iodide (PbI_2) (≥99.5%) methylammonium iodide (MAI) (99.9%) were purchased from Xi'an Polymer Light Technology Corp, N, N-dimethylformamide (DMF) (99.8%), dimethyl sulfoxide (DMSO) (99.9%), chlorobenzene (CB) (99%), ethyl acetate (99.5%) and $SnCl_2 \cdot 2H_2O$ (99.99%) were obtained from Aladdin. FTO substrates were purchased from Ying Kou OPV Tech New Energy Co., Ltd., and Coal comes from Dahuangshan coal mine in Xinjiang, China. All chemical reagents were of analytical grade and used without further purification.

1.2 Preparation of coal-based F/N-GQDs

Coal-based F/N-GQDs were synthesized by our previously reported method[16] as shown in Figure 1(a). In short, the coal was pretreated and then condensed and refluxed with H_2O_2 solution. After the condensing reflux was completed, the excess H_2O_2 solution was removed to obtain the F/N-GQDs aqueous solution. Then the solution was transferred to a 100 mL Teflon lined stainless steel autoclave, and 0.4 mol L^{-1} HF solution was added and kept at 120 ℃ for 10 h. After that, the autoclave was naturally cooled down to room temperature. The obtained suspension was dialysised via a 0.22 μm filter to remove large particles, and the purified solution is freeze-dried to obtain F/N-GQDs powder.

1.3 Device fabrication

In detail, the FTO glass substrate was continuously ultrasonicated in succession with deionized water (DI), isopropanol (IPA), and ethanol for 20 min,, respectively.

Then it was dried by hot-air flowing and treated with a UV/ozone for 15 min. Next, SnO_2 precursor was spin-coated on the cleaned FTO substrate at 3000 rpm for 30 s and thermally annealed on a hot plate at 200℃ for 60 min in ambient air. After that, the 159 mg MAI and 461 mg PbI_2 were dissolved in a mixed solvent of 0.7 mL anhydrous DMF and DMSO (9:1, V/V) to obtain perovskite precursor solution. After cooling to room temperature, the obained films were treated with UV/ozone for 15 min. The perovskite precursor was then deposited on the substrate at the speed of 4000 rpm for 30 s. Then 450 μL ethyl acetate (without/with F/N-GQDs) was dropped at the center of the spinning substrate for 17 s before the end of spin-coating. For the post-treatment passivation of perovskite films, F/N-GQDs IPA solution was spin-coated at 3000 rpm for 30 s, followed by annealing at 80°C for 10 min. Subsequently, the commercial carbon paste (Japan JUJO chemical Co., Ltd) was coated on the perovskite layer with a thickness controlled by two layers of polyimide tape (60 μm), and the total thickness is 120 μm, and dried at 60℃ for 10 min. The above operation was repeated twice to form CEs and complete the device preparation. All device fabrication processes were carried out under air condition with a temperature range of 20-25 ℃ and a relative humidity of 10-20%.

1.4 Characterizations

Microstructure of the F/N-GQDs was characterized by a high-resolution transmission electron microscopy (HRTEM, FEI Talos F200S). Both ultraviolet photoemission spectroscopy (UPS) and X-ray photoelectron spectroscopy

(XPS) analyses were performed by using a photoelectron spectrometer (Thermo Fisher, Escalab 250Xi). Steady-state Photoluminescence (PL) and time-resolved photoluminescence (TRPL) were all performed by FLS980 (Edinburgh Instruments Ltd.) with a picosecond pulsed diode laser (EPL-475) to study the carrier transport kinetics. Raman test was carried out using French HORIBA Scientific (Lab-RAM HR Evolution). Surface morphologies of the perovskite films and devices cross-sections were characterized by a field emission scanning electron microscope (SEM, SU8010, Hitachi), and the grain size of the perovskite film in the SEM image was measured by software (Nano Measurer). Wettability was analyzed using a contact angle analyzer (Dataphysics OCA20). Atomic force microscope (AFM, Bruker, Dimension Fast Scan) was used to analyze the surface roughness of the perovskite films. Crystallographic properties were characterized by X-ray diffraction (XRD, D8 Advance, BRUKER) at *Cu* K_α radiation of 40 mA and 45 kV (λ =1.54056 Å) in the range of 15-50◦. *J-V* curves of C-PSCs were obtained in ambient air using a Keithley 2400 source meter under irradiation of simulated solar light intensity controlled at AM 1.5 G (100 mW cm^{-2}). Light intensity was calibrated by a standard silicon solar cell that NREL certified. The effective area of C-PSCs was 0.08 cm^2, which was defined using a black metallic mask. The electrochemical impedance spectroscopy (EIS) was carried out by CHI660D electrochemical workstation from 0.1 MHz-0.1 Hz frequency at a bias voltage of 0.8 V in the dark and its Nyquist curve was fitted by the Z-view software. TPV measurement was performed with a system excited by a 532 nm (1000 Hz, 3.2 ns) pulse laser. Before

testing, the devices were connected with a digital oscilloscope (DOS-X 3104A) and the internal impedance of the digital oscilloscope is set to 1MΩ to form an open-circuit condition. During the testing, the solar simulator provided steady-state illumination of 100 mW cm^{-2}.

2 Supporting Figures

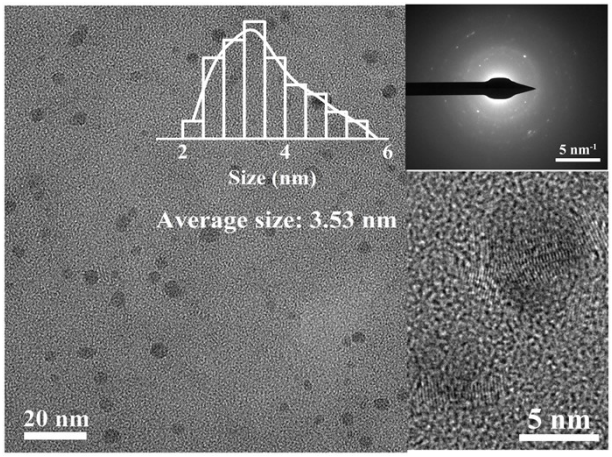

Fig. S1. HR-TEM image of F/N-GQDs; Inset: the histogram of lateral size distribution.

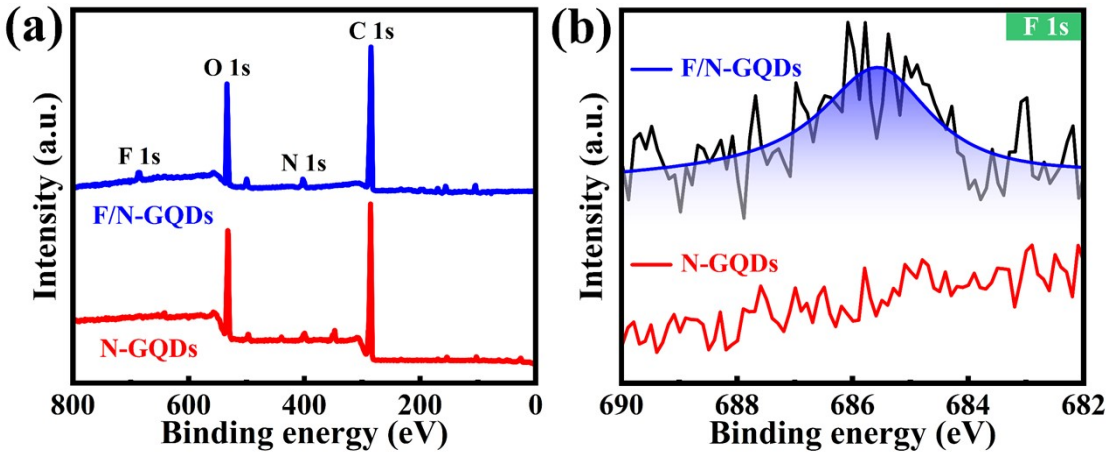

Fig. S2. (a) XPS survey spectrum of N-GQDs and F/N-GQDs. (b) The corresponding high resolution XPS spectra of F 1s.

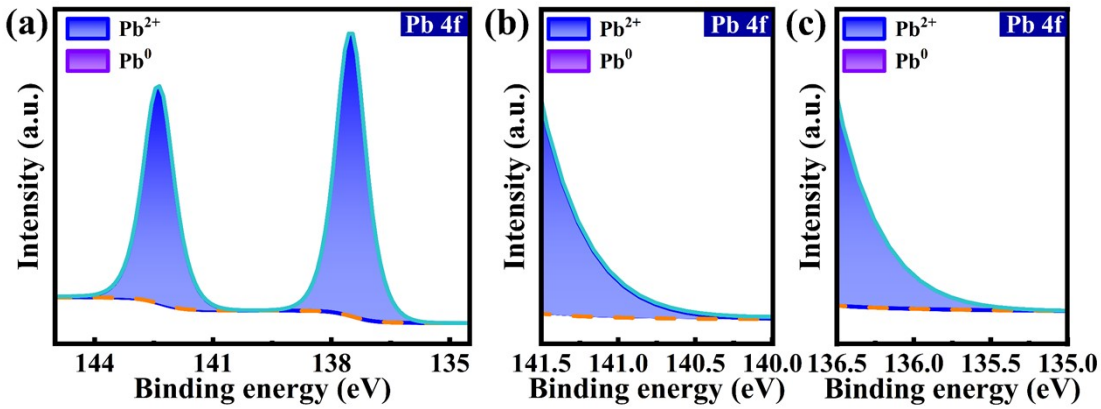

Fig. S3. (a) The corresponding high-resolution XPS spectra of Pb 4f from Dual film.

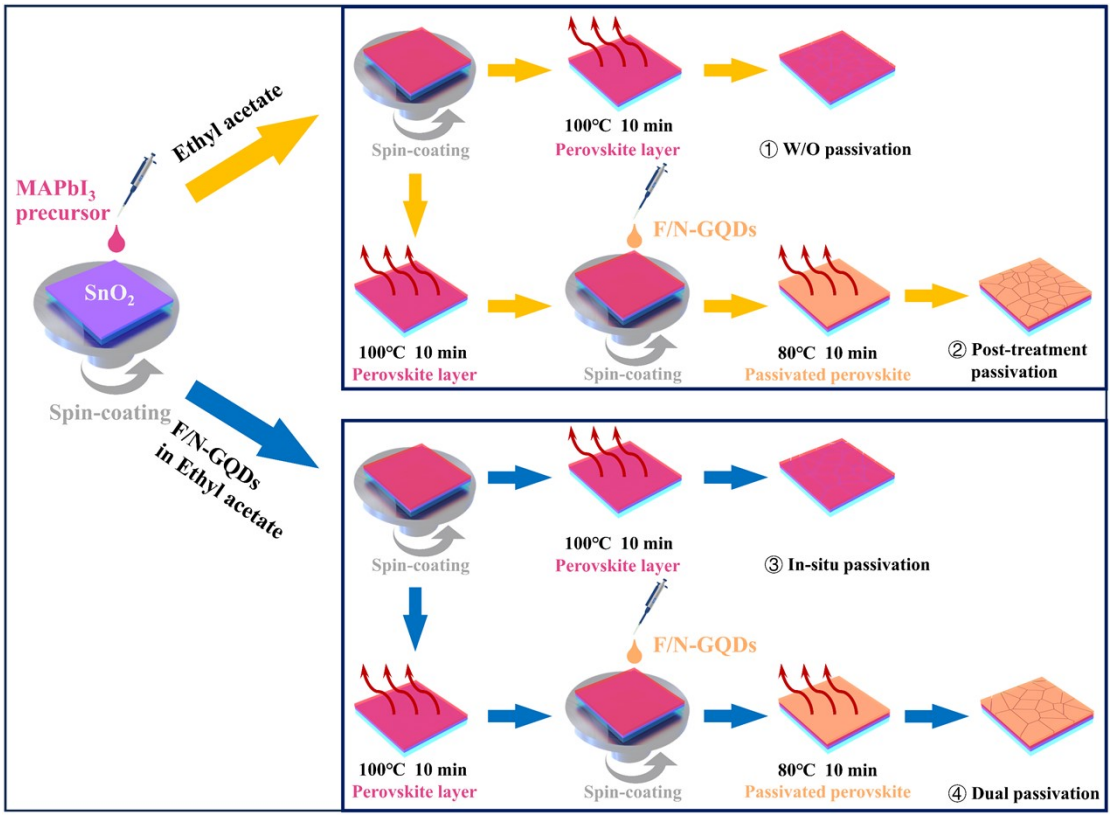

Fig. S4. Schematic diagram of perovskite film fabrication via In-situ passivation strategy, Post-treatment passivation strategy and Dual passivation strategy.

The corresponding films/devices based on the pristine $MAPbI_3$, $MAPbI_3$ treated with in-situ passivation, post-treatment passivation, and dual passivation strategy are abbreviated to the Pristine film/device, In-situ film/device, Post film/device, and Dual film/device, respectively.

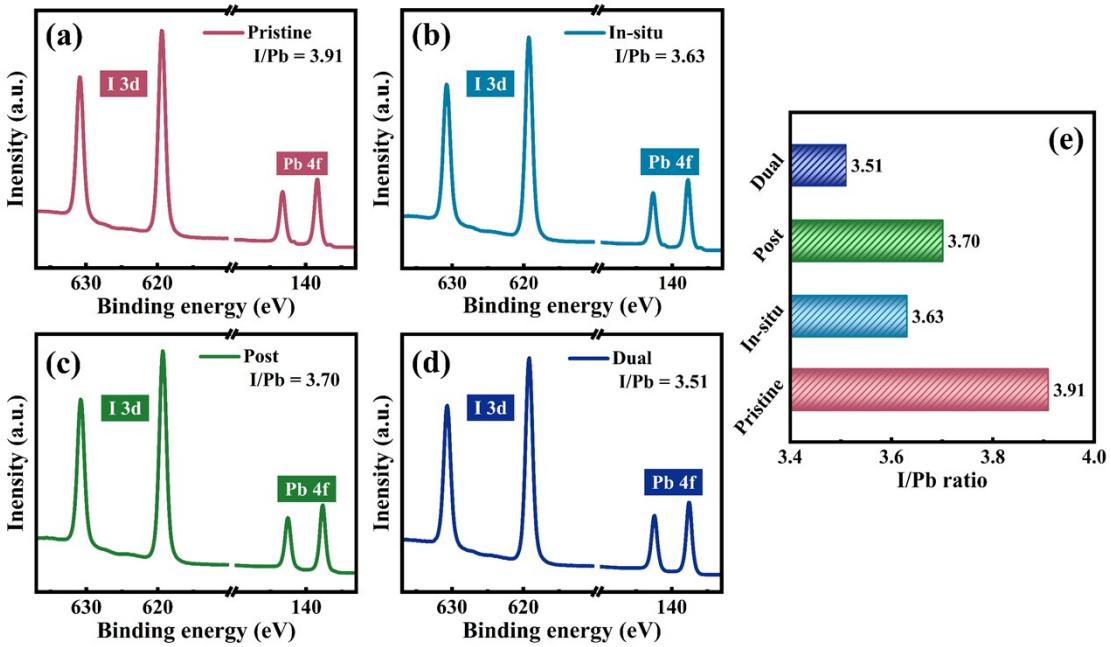

Fig. S5. XPS spectra of the (a) Pristine (b) In-situ (c) Post and (d) Dual films. (e) I/Pb ratio from XPS data.

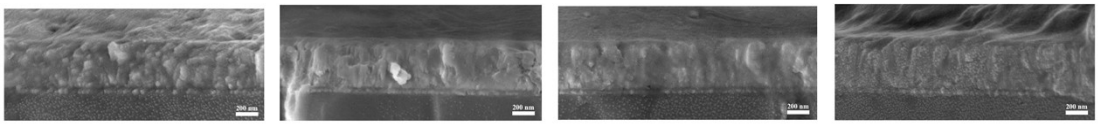

Figures S6. Cross-section SEM images of different perovskite films.

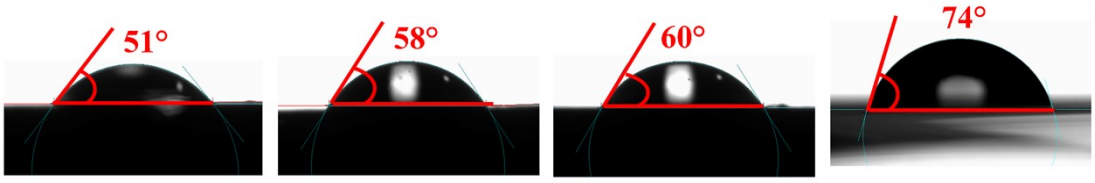

Fig. S7. Water contact angles of different perovskite films.

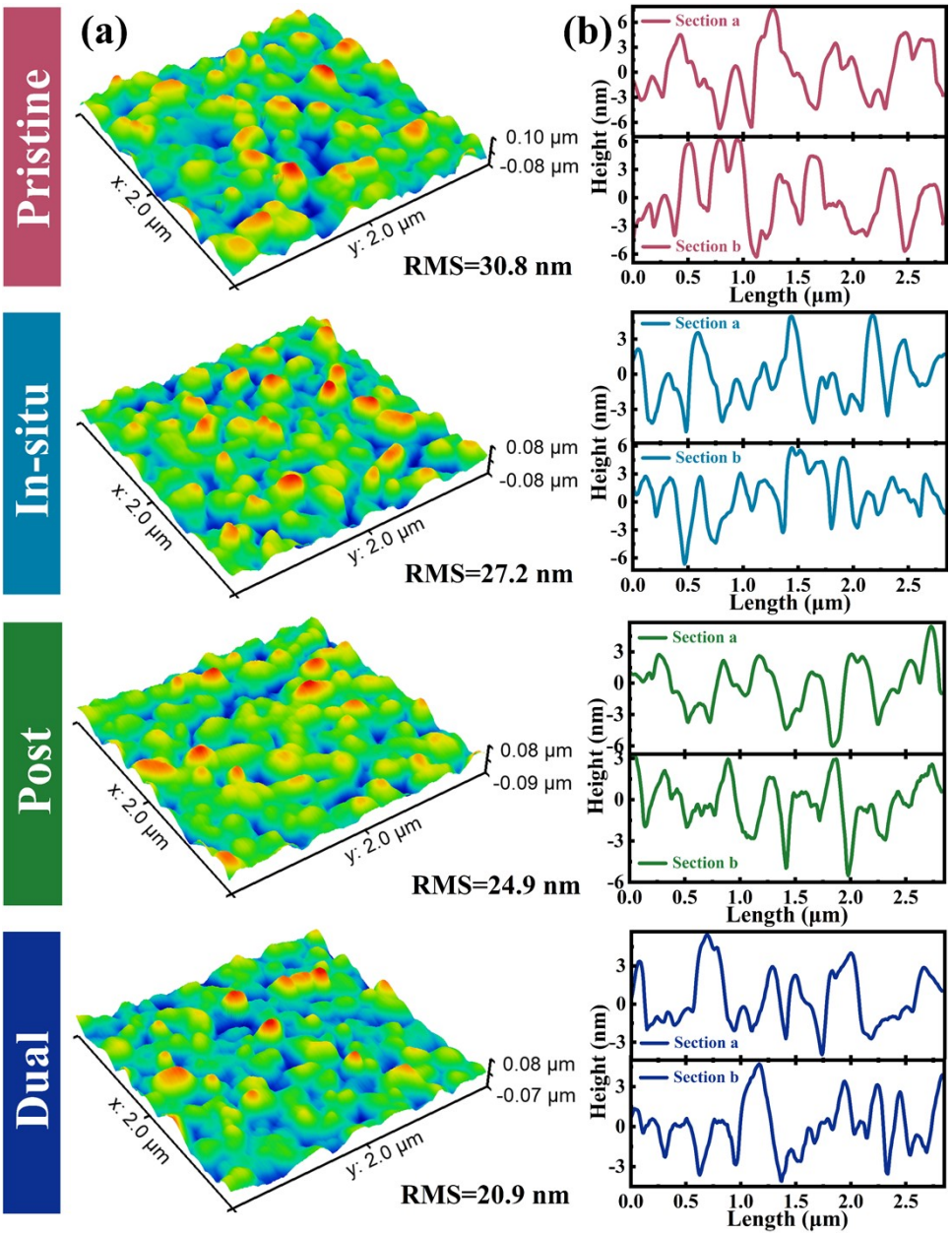

Fig. S8. (a) 3D AFM images of different perovskite films; (b) The height curves vary with distance are recorded from the solid line of the corresponding 2D AFM image.

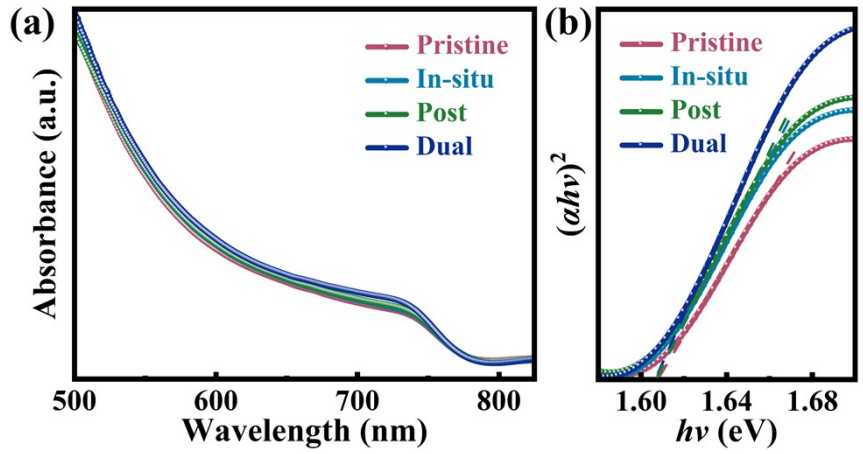

Fig. S9. (a) UV-Vis absorption spectra and (b) Tauc plots of different perovskite films.

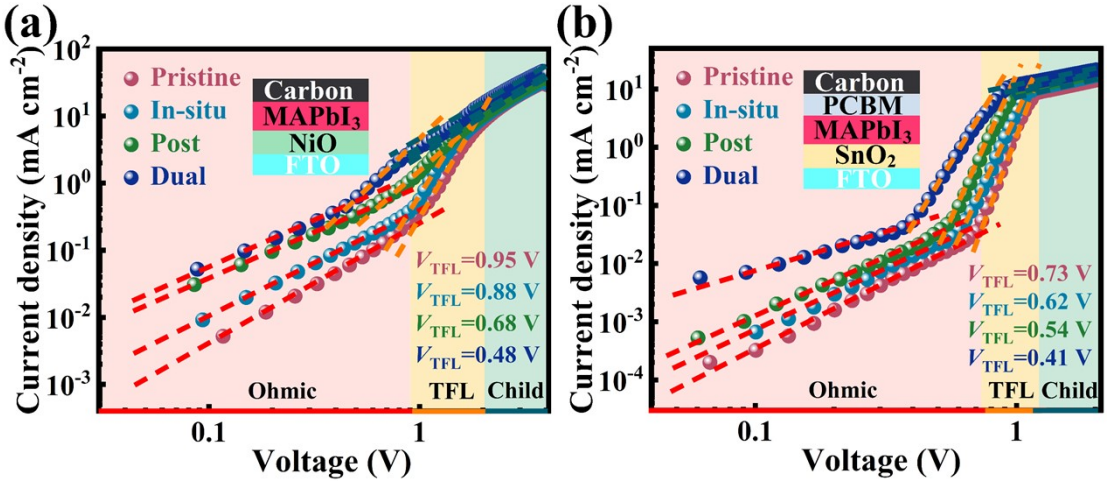

Fig. S10. Dark *J*-*V* curves from (a) hole-only and (b) electron-only devices based on different perovskite films.

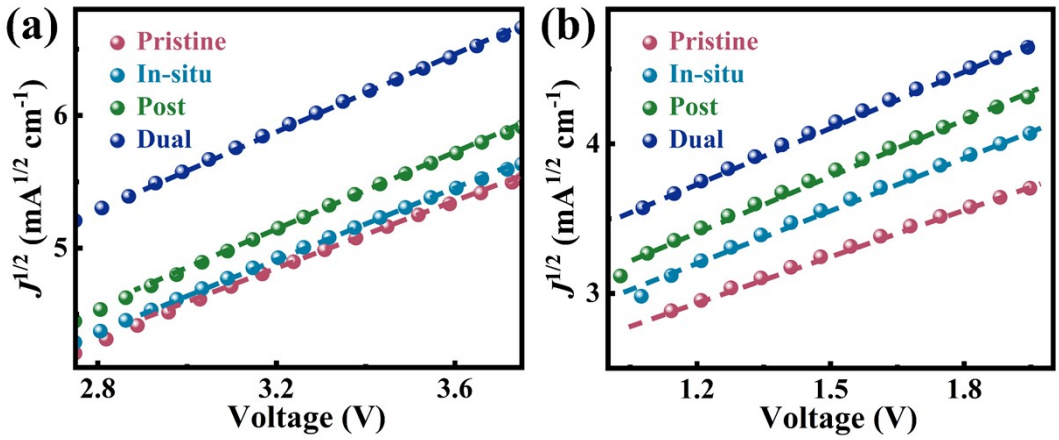

Fig. S11. $J^{1/2}$-*V* curves from (a) hole-only and (b) electron-only devices based on different perovskite films.

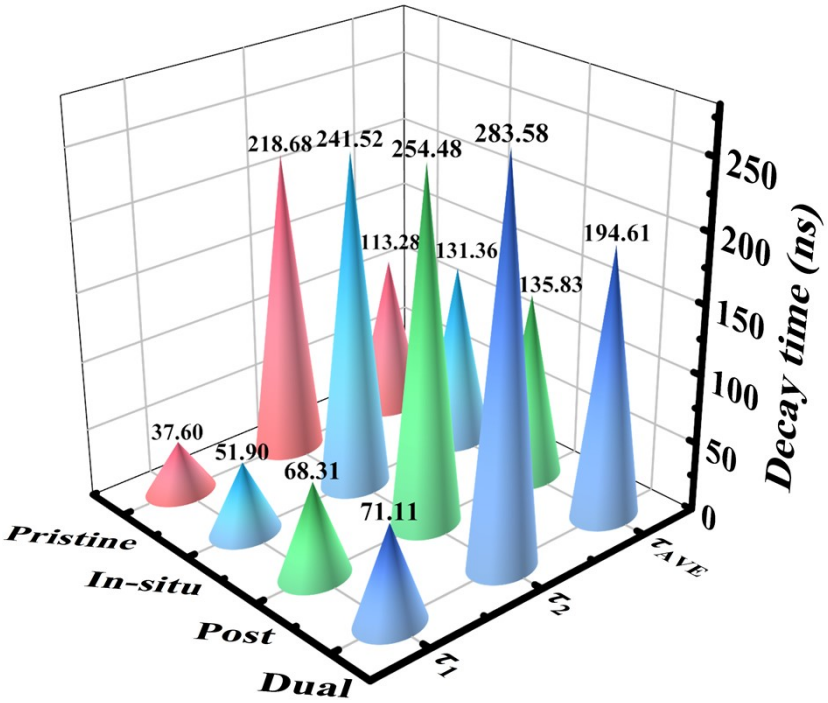

Fig. S12. Carrier lifetime of four kinds of perovskite films on glass substrates.

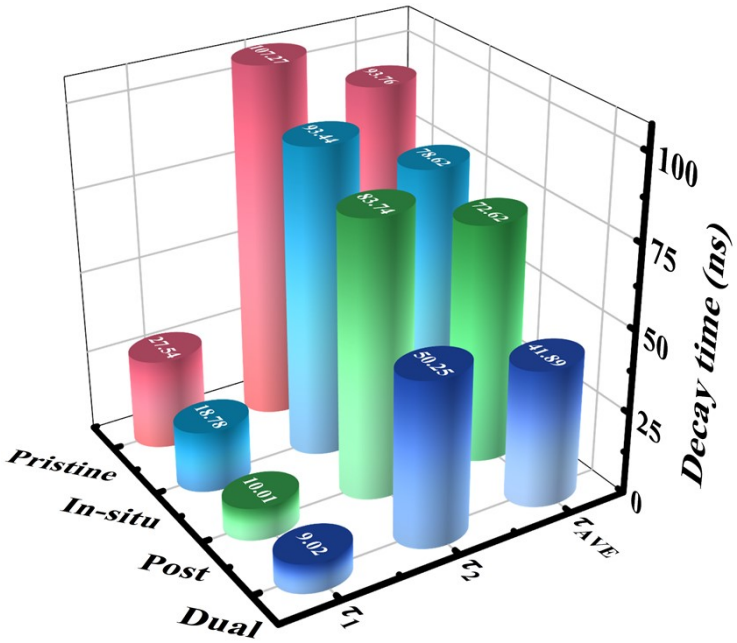

Fig. S13. Carrier lifetime of four kinds of perovskite films covered by the CEs.

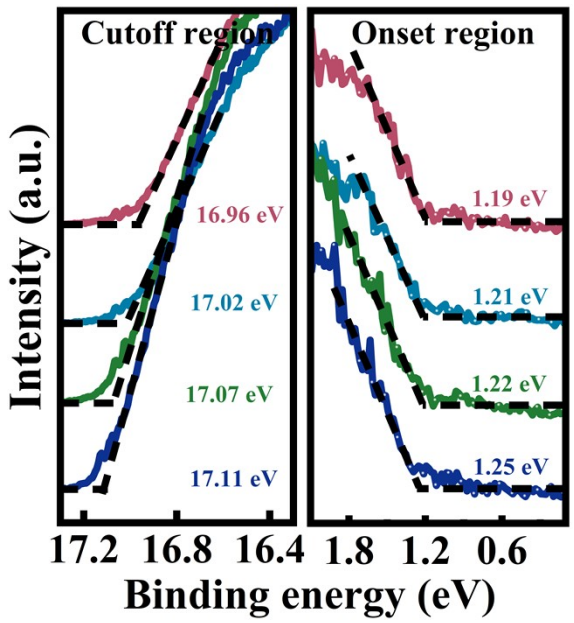

Fig. S14. UPS spectra of different perovskite films.

The passivation treatment of F/N-GQDs may also influence work function of perovskite films and the interface energy level alignment in the devices, where the energy level alignment is another key factor in determining the charge transport behaviors.

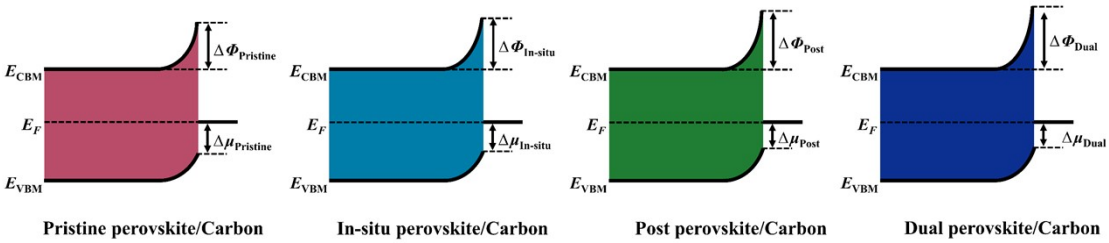

Fig. S15. Schematic illustration of the Perovskite/Carbon interface.

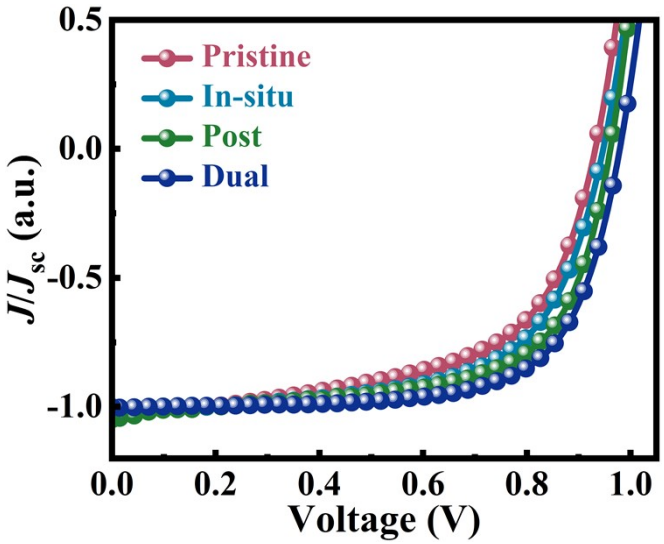

Fig. S16. The *J-V* curves are normalized by J_{sc} values.

The high field and the low field represents the short circuit (SC) and the open circuit (OC) condition, respectively, to compare the field dependent behavior from SC to MPP. At SC, the steep slope suggests that the charge collection is strongly field dependent.

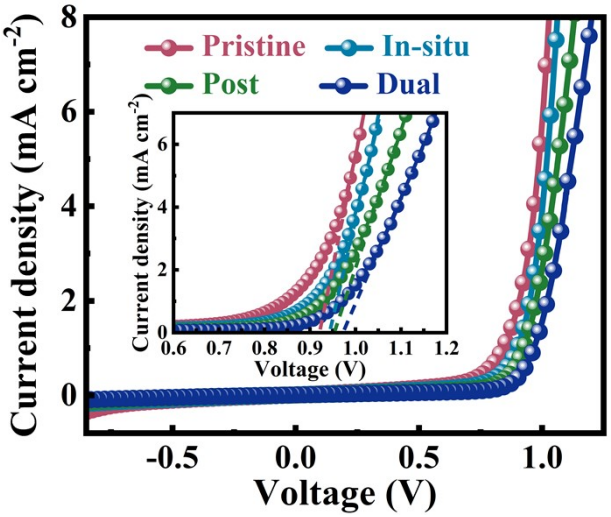

Fig. S17. The curve of dark *J-V*.

Based on the intercept between the linear part of the curves and the horizontal axis, the values of V_{oc} can be estimated to be 0.923 V (Pristine device), 0.944 V (In-situ device), 0.957 V (Post device) and 0.976 V (Dual device), respectively, confirming that the passivated devices have a higher intrinsic V_{oc}[1].

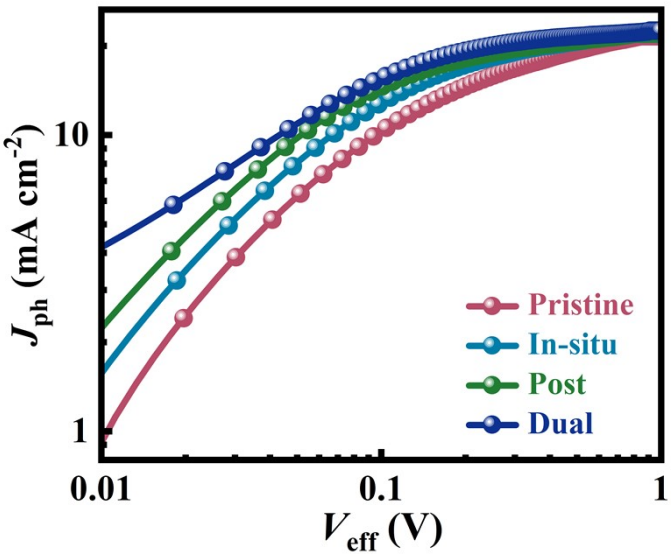

Fig. S18. Plots of J_{ph} with respect to the V_{eff}.

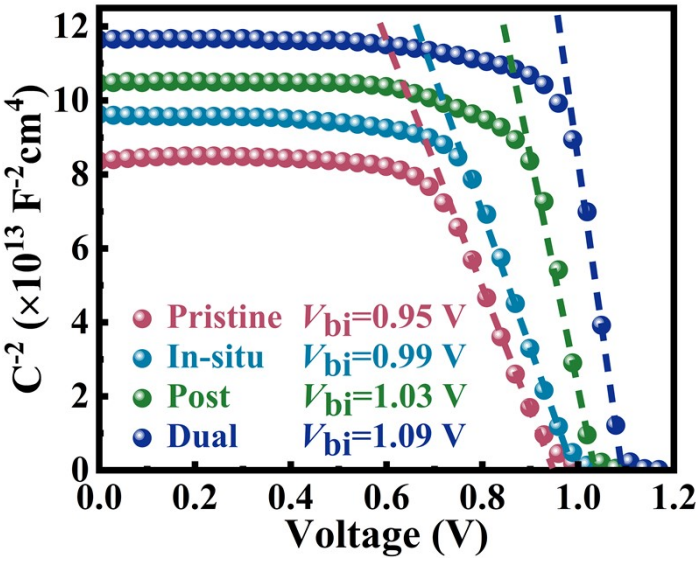

Fig. S19. Mott-Schottky plots of devices based on different perovskite layers.

The *C*-*V* measurements under dark conditions was analyzed using Mott-Schottky equation:

$$\frac{1}{C^2} = \frac{2}{q\varepsilon\varepsilon_0 N}(V - V_{bi} - \frac{K_B T}{q})$$

where the built-in potential (V_{bi}) can be xtracted from the intercept of C^{-2} versus the applied voltage V, and the charge carrier density can be obtained from the slope, thereby revealing the accumulation/extraction of charge between the perovskite

layer/CE.

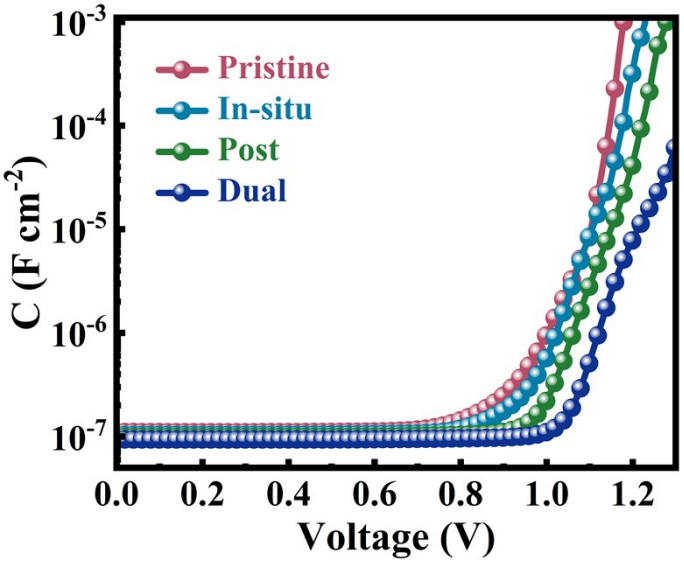

Fig. S20. *C-V* curves of devices based on different perovskite layers

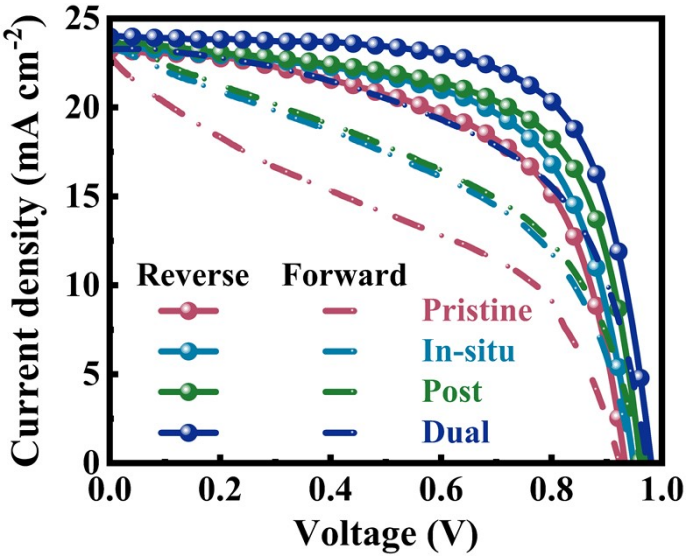

Fig. S21. *J-V* curves scanned both forward and reverse directions of devices based on different perovskite films.

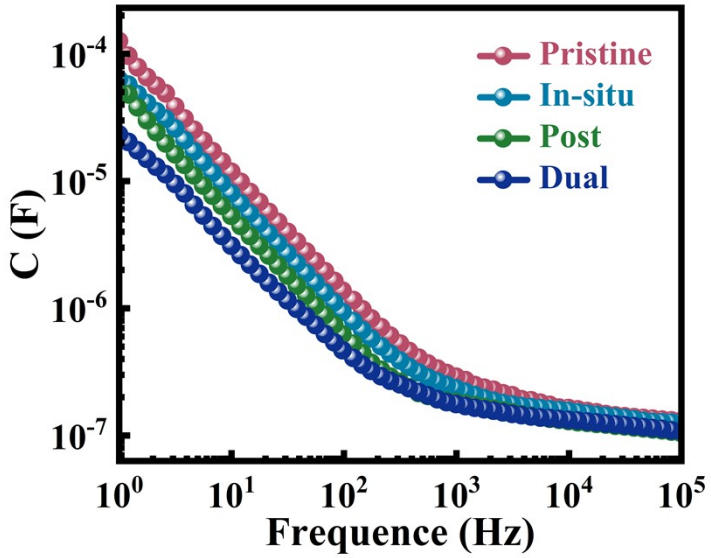

Fig. S22. *C-F* curves of devices measured at a reverse potential of 0.8 V

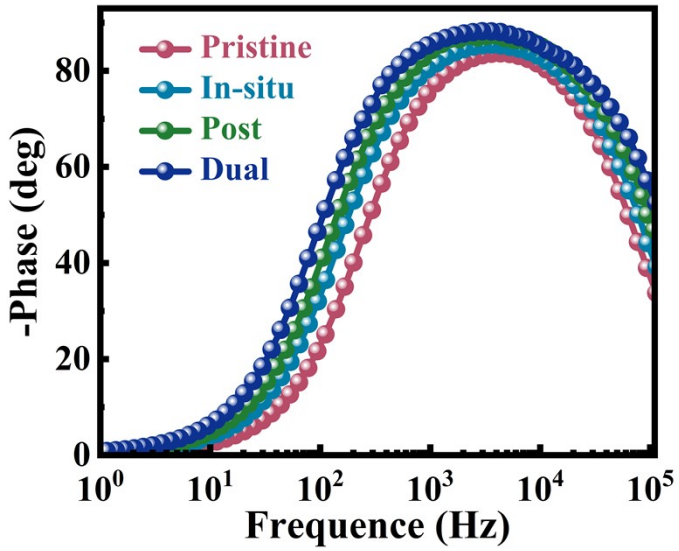

Fig. S23. Bode curves of devices measured at a reverse potential of 0.8 V

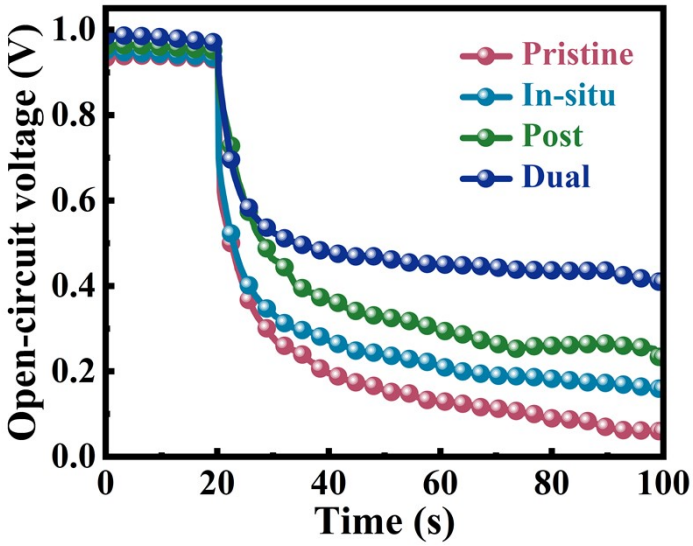

Fig. S24. OCVD of devices based on different perovskite films.

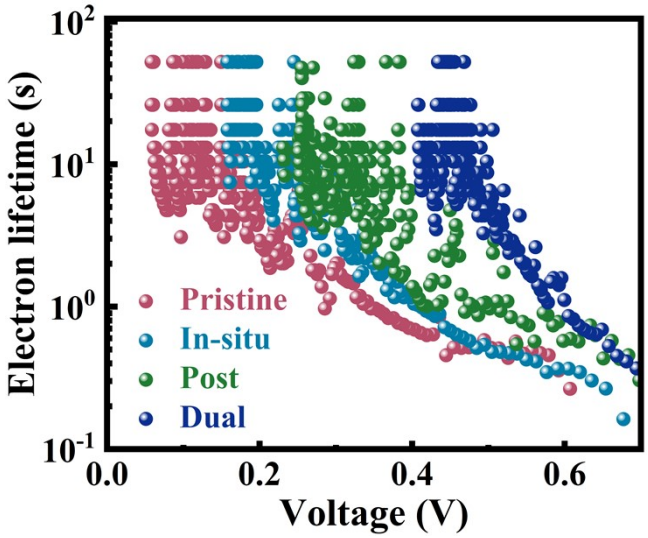

Fig. S25. Electron lifetime curves of devices based on different perovskite films.

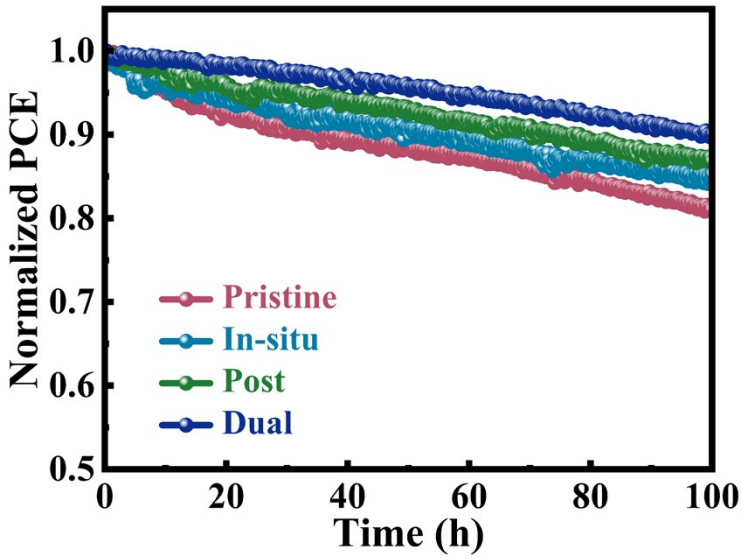

Fig. S26. The long-term stability of unpackaged C-PSCs under continuous MPP tracking.

3 Supporting Tables

Sample	A_1 (%)	τ_1 (ns)	A_2 (%)	τ_2 (ns)	τ_{AVE} (ns)
Pristine	89.01	37.60	10.99	218.68	113.28
In-situ	86.58	51.90	13.42	241.52	131.36
Post	86.75	68.31	13.25	254.48	135.83
Dual	74.18	71.11	25.82	283.58	194.61

Tables S1. TRPL fitting parameters of perovskite films deposited on glass substrate.

Sample	A_1 (%)	τ_1 (ns)	A_2 (%)	τ_2 (ns)	τ_{AVE} (ns)
Pristine	44.27	27.54	55.73	107.27	93.76
In-situ	55.20	18.78	44.80	93.44	78.62
Post	59.78	10.01	40.22	83.74	72.62
Dual	58.63	9.02	41.37	50.25	41.89

Tables S2. TRPL fitting parameters of perovskite films covered by the CEs.

Device		V_{oc} (V)	J_{sc} (mA cm^{-2})	FF (%)	PCE (%)
Pristine	Best	0.935	22.88	60.17	12.87
	Average	0.932±0.005	22.46±0.30	56.39±2.44	11.80±0.59
In-situ	Best	0.949	22.96	64.36	14.04
	Average	0.947±0.004	22.80±0.24	61.63±1.62	13.30±0.39
Post	Best	0.963	23.05	66.56	14.77
	Average	0.956±0.006	23.04±0.27	63.51±1.49	13.99±0.37
Dual	Best	0.983	23.88	69.88	16.37
	Average	0.977±0.006	23.37±0.27	67.12±1.78	15.34±0.50

Tables S3. Summary of the performance photovoltaic parameters of different devices.

4 Supporting Notes

Note S1. Williamson-Hall analysis

The lattice strain and crystallite size of perovskite films were calculated from XRD patterns using the Williamson-Hall analysis[2]:

$$\beta\cos\theta = 4\varepsilon\sin\theta + \frac{K\lambda}{D} \tag{9}$$

Where β is the full width at half maximum (FWHM) of XRD peaks, θ is diffraction angle, ε is the slope of the straight line, representing lattice strain, K is shape factor (0.9), λ is wavelength of X-ray source (0.15418 nm) and D is crystallite size. By linear fitting $\beta\cos\theta$ as a function of $4\sin\theta$, the lattice strain and the crystallite size can be derived from the slope (ε) and intercept ($\frac{K\lambda}{D}$) of the fitted line, respectively.

Note S2. Urbach energy calculation

Urbach energy (E_u) can be calculated from the UV-vis absorption spectra of the films with this formula[3]:

$$\alpha = \alpha_0 \exp(h\nu/E_u) \tag{6}$$

Where α is absorption coefficient (cm^{-1}), α_0 is a constant and $h\nu$ is photon energy (eV).

Note S3. Space-charge-limited-current (SCLC) analysis

Space charge limited current (SCLC) measurements were performed on hole-only device based on the FTO/NiO/$MAPbI_3$/CE structure and electron-only device based on the FTO/SnO_2/$MAPbI_3$/PCBM/CE structure, the hole/electron trap state density (N_{trap}) and carrier mobility (μ) of the pristine and F/N-GQDs passivated perovskite films were quantitatively analyzed. Among them, NiO was prepared and spin-coated following the literature[4]. The N_{trap} of perovskite film can be measured using the following equation[5]:

$$N_{trap} = \frac{2\varepsilon_0\varepsilon_r V_{TFL}}{qL^2} \tag{1}$$

Where ε_0, ε_r, and L are vacuum permittivity, relative permittivity, and the thickness of the perovskite film, respectively, and q is elemental charge. And μ of the four kinds

of perovskite films were calculated using the Mott-Gurney equation[6]:

$$\mu = \frac{8L^3 J_D}{9\varepsilon\varepsilon_0 V^2} \quad (2)$$

Where J_D is current density and V is bias voltage.

Note S4. Thermal admittance spectroscopy (TAS) analysis

The trap density (N_T) can be estimated from the angular frequency dependent capacitance using the following equation:

$$N_T(E_\omega) = -\frac{V_{bi}\mathrm{d}C\ \omega}{qW\mathrm{d}\omega k_B T} \quad (7)$$

Where V_{bi} denotes built-in potential, W is depletion width, C is capacitance, ω is frequency, k_B is Boltzmann constant, and T is temperature. V_{bi} and W are obtained from the Mott-Schottky plots. The applied angular frequency ω defines the energetic demarcation, according to the following equation[7]:

$$E_\omega = k_B T \ln(\frac{\omega_0}{\omega}) \quad (8)$$

Where ω_0 is attempt-to-escape frequency.

Note S5. Time-resolved photoluminescence (TRPL) measurements and the calculation of carrier lifetimes

The TRPL decay curves were fitted using the following biexponential decay function (ExpDec2)[8]:

$$f(t) = A + B_1\exp(-t/\tau_1) + B_2\exp(-t/\tau_2) \quad (3)$$

where τ_1 and τ_2 represent the carrier lifetimes for fast and slow recombination processes, and B_1, B_2 and A are fitting parameters, respectively. The average carrier lifetime (τ_{AVE}) can be calculated according to the following formula[8]:

$$\tau_{AVE} = (\sum B_i\tau_i^2)/(\sum B_i\tau_i) \quad (4)$$

Note S6. Calculation of carrier diffusion length (L_D)

For PSCs, L_D is another key factor in characterizing the carrier transport ability, which. We quantified hole diffusion lengths in the perovskite films. L_D can be

estimated according to the 1D diffusion equation[9]:

$$\frac{\tau}{\tau_0} = 1 + \frac{\pi^2}{4} \times \left(\frac{L_D}{L}\right)^2 \quad (5)$$

where L_D is the diffusion length, τ and τ_0 represent the carrier lifetime of the perovskite film without and with a carbon layer, respectively.

Note S7. Ultraviolet photoelectron spectroscopy (UPS) analysis

The UPS analyse was performed by Thermo Fisher, Escalab 250Xi. He I (hv = 21.22 eV) emission source is employed. Figure S14 (left panel) shows the secondary electron cutoff spectra of all the perovskite films, from which the work function (WF) can be obtained using the equation[10]:

$$\mathrm{WF} = hv - E_{\mathrm{cutoff}}$$

where hv is the photoelectron energy of He I light, and E_{cutoff} is the secondary electron cutoff. The valence band maximum (VBM) and conduction band minimum (CBM) of the perovskite films sample can be calculated by the

$$\mathrm{VBM} = 21.22\ \mathrm{eV} - (E_{\mathrm{cutoff}} - E_{\mathrm{onset}}) \quad (10)$$

$$\mathrm{CBM} = \mathrm{VBM} + E_g \quad (11)$$

where the E_g is the bandgap calculated by UV-vis measurements.

Note S8. Analysis of the slopes of the normalized *J-V* curves at each voltage

Ideally, under OC conditions, an almost vertical steep curve represents a rapid transition from MPP to OC, indicating efficient photocurrent collection. The increased charge collection at OC is also reflected as charge collection at SC that is less field dependent, since the highly steep slope near OC indicates desirable charge collection efficiency even at the low-field regime, showing a field independent charge collection property[11]. At SC, the charge collection relies on electron-hole pair separation (exciton dissociation) followed by transport drifting by the internal field. Their slopes at SC remains nearly unchanged, indicating similar drift transport for all films because of the presence of a large internal field. In contrast, at OC, the internal field is low and the charge collection relies more on carrier diffusion. Consequently, any potential insulator

or trap states in the active layer or at the interfaces would appreciably deteriorate the charge collection efficiency[12]. At the same time, a high V_{oc} value is also an indication of low nonradiative recombination at OC.

Note S9. Photocurrent density (J_{ph}) versus effective voltage (V_{eff}) analysis

J_{ph} and V_{eff} are defined as follows:

$$J_{ph}=J_L-J_D \tag{13}$$

$$V_{eff}=V_0-V \tag{14}$$

where J_L and J_D are the current densities under AM 1.5G 100 mW cm^{-2} illumination and in the dark, respectively. V is applied voltage, and V_0 is voltage when J_{ph}=0. In the lower V_{eff} region, the J_{ph} of the four devices increases sharply with the increase of V_{eff}, while in the higher V_{eff} region, J_{ph} gradually reaches J_{sat}, indicating that almost all of the excitons can be dissociated into free carriers, and no charge recombination occurs before being collected by the electrode. Generally, the saturation current density (J_{sat}) is related to the maximum exciton generation rate (G_{max}), the G_{max} of the devices were assessed using the equation of $G_{max}=J_{sat}/qL$[13], where the q and L denote the electronic charge (1.6×10^{-19} C) and the thicknesses of the film (425 nm in this study), respectively. The values of G_{max} for the Pristine, In-situ, Post, and Dual devices are 1.45×10^{28}, 1.54×10^{28}, 1.78×10^{28}, and 2.24×10^{28} m^{-3} s^{-1}, respectively.

Note S10. Calculations of R_s, A and J_0 from J-V curves

A planar structured PSC can be treated as a single junction diode with a large shunt resistance, and its J-V curve can be described as[14]:

$$J = J_{sc} - J_0\{\exp[\frac{e(V+JR_s)}{AK_BT}]-1\} \tag{15}$$

where J is the current flow through the external load, J_{sc} is photo-induced current density, J_0 is dark saturate current density, V is applied voltage, A is ideality factor, K_B is Boltzmann constant, T is temperature, and e is electron charge. Equation (11) can

also be transformed into the following equation[14]:

$$-\frac{\mathrm{d}V}{\mathrm{d}J}=\frac{AK_{\mathrm{B}}T}{e}(J_{\mathrm{sc}}-J)^{-1}+R_{\mathrm{s}} \tag{16}$$

A and R_{s} can be obtained from the slope of the -dV/dJ vs $(J_{\mathrm{sc}}-J)^{-1}$ curves and the intersection of the curves with the ordinate. Based on to equation (16), V_{oc} can be expressed as in the following equation[14]:

$$V_{\mathrm{oc}}=\frac{AK_{\mathrm{B}}T}{e}\ln\left(\frac{J_{\mathrm{sc}}}{J_0}+1\right) \tag{17}$$

The above equation shows that J_0 and A can be obtained by fitting the linear part in region Ⅱ of the dark J-V curves.

Note S11. Open-circuit photovoltage decay (OCVD) measurements

First, the device was illuminated at open-circuit for 20 s to achieve the photostationary state, and when the light was instantaneously switched off, the photocarriers underwent rapid recombination, the recombination process can be clearly reflected through the OCVD measurements. And the corresponding electron lifetime (τ_{n}) of the devices also can be extracted based on the following formula[15]:

$$\tau_n=-\frac{K_{\mathrm{B}}T}{e}\left(\frac{\mathrm{d}V_{\mathrm{oc}}}{\mathrm{d}t}\right)^{-1} \tag{12}$$

where K_{B} is the Boltzmann constant, T is the absolute temperature, e is the electron charge, and dV_{oc}/dt is the derivative of the open-circuit photovoltage transient.

5 References for Supporting Information

1. S. Zhong, Z. Li, C. Zheng, X. Luo, J. Gao, X. Lu, X. Gao, L. Shui, S. Wu and J.-M. Liu, *Sol. RRL*, 2022, **6**, 2200088.
2. X. Li, Z. Ying, J. Zheng, X. Wang, Y. Chen, M. Wu, C. Xiao, J. Sun, C. Shou, Z. Yang, Y. Zeng, X. Yang and J. Ye, *Adv. Mater.*, 2023, **35**, 2211962.
3. J. Park, J. Kim, H.-S. Yun, M. J. Paik, E. Noh, H. J. Mun, M. G. Kim, T. J. Shin and S. I. Seok, *Nature*, 2023, **616**, 724–730.
4. Y. Ma, H. Zhang, Y. Zhang, R. Hu, M. Iiang, R. Zhang, H. Lv, J. Tian, L. Chu, J. Zhang, Q. Xue, H.-L. Yip, R. Xia, X. a. Li and W. Huang, *ACS Appl. Mater. Interfaces*, 2019, **11**, 3044-3052.
5. Y. Luo, K. Liu, L. Yang, W. Feng, L. Zheng, L. Shen, Y. Jin, Z. Fang, P. Song, W. Tian, P. Xu, Y. Li, C. Tian, L. Xie and Z. Wei, *Nat. Commun.*, 2023, **14**, 3738-3738.
6. Y. Yang, Y. Wang, Z. Qu, K. Zhang, T. Liang, S. Chen, W. Lv, F. Min, Y. Chen, Y. Qiao and Y. Song, *Angewandte Chemie-International Edition*, 2023, **62**, e202300971.
7. J. A. Hong, M. Jeong, S. Park, A.-Y. Lee, H. S. Kim, S. Jeong, D. W. Kim, S. Cho, C. Yang and M. H. Song, *Adv. Sci.*, 2022, **10**, 2205127.
8. J. Guo, B. Wang, D. Lu, T. Wang, T. Liu, R. Wang, X. Dong, T. Zhou, N. Zheng, Q. Fu, Z. Xie, X. Wan, G. Xing, Y. Chen and Y. Liu, *Adv. Mater.*, 2023, **35**, 2212126.
9. Y. Li, Z. Chen, B. Yu, S. Tan, Y. Cui, H. Wu, Y. Luo, J. Shi, D. Li and Q. Meng, *Joule*, 2022, **6**, 676-689.
10. Z. Iqbal, F. Zu, A. Musiienko, G.-P. Emilio, H. Köbler, T. W. Gries, G. V. Sannino, L. Canil, N. Koch, M. Stolterfoht, D. Neher, M. Pavone, A. B. Muñoz-García, A. Abate and Q. Wang, *ACS Energy Lett.*, 2023, **8**, 4304–4314.
11. J. Li, R. Munir, Y. Fan, T. Niu, Y. Liu, Y. Zhong, Z. Yang, Y. Tian, B. Liu, J. Sun, D.-M. Smilgies, S. Thoroddsen, A. Amassian, K. Zhao and S. F. Liu, *Joule*,

2018, **2**, 1313–1330.

12. H. Tsai, R. Asadpour, J.-C. Blancon, C. C. Stoumpos, J. Even, P. M. Ajayan, M. G. Kanatzidis, M. A. Alam, A. D. Mohite and W. Nie, *Nat. Commun.*, 2018, **9**, 2130.
13. R. K. Gunasekaran, J. Jung, S. W. Yang, J. Yun, Y. Yun, D. Vidyasagar, W. C. Choi, C.-L. Lee, J. H. Noh, D. H. Kim and S. Lee, *Infomat*, 2023, **5**, e12393.
14. J. You, Y. Yang, Z. Hong, T.-B. Song, L. Meng, Y. Liu, C. Jiang, H. Zhou, W.-H. Chang, G. Li and Y. Yang, *Appl. Phys. Lett.*, 2014, **105**, 183902.
15. C. Geng, P. Wei, H. Chen, H. Liu, S. Zheng, H. Wang and Y. Xie, *Chem. Eng. J.*, 2021, **414**, 128878.